UNIVERSITÀ DEGLI STUDI DI PADOVA

Dipartimento di Fisica e Astronomia "Galileo Galilei"

Corso di Laurea in Fisica

Tesi di Laurea

Sensitivity of a Compton nanosatellite for Gamma-Ray Burst observations

Relatore
Prof. Riccardo Rando

Laureando
Sofia Canevarolo

Anno Accademico 2017/2018

Contents

Introduction

A turning point for multi-messenger astrophysics, which consists on the simultaneous observation of astronomical signals with particles of different nature, is the famous, first measurement of gravitational waves and electromagnetic radiation from the same astrophysical source, dated on August 17, 2017.
That day, the gravitational signal was detected by the Laser Interferometer Gravitational-Wave Observatory (LIGO); approximately 1.7 s after the Fermi Gamma-ray Burst Monitor (GBM) triggered a short Gamma-Ray Burst, GRB 170817A. In addition, the GRB signal was independently confirmed by the INTernational Gamma-ray Astrophysics Laboratory (INTEGRAL) with a measurement provided by the SPI-ACS instrument on board.

The localization of GRB 170817A sent by GBM was not particularly precise: the 90% probability region covered about 1800 square degrees. Therefore, the information provided by GBM results only in a little improvement from the localization individualized by the LIGO and Virgo detectors, whose 90% confidence region spanned 31 square degrees. Anyway, through the intersection of the two probability region, a better localization of the source was possible [4].
The large localization region of GBM was due to both the weak nature of the GRB and the high backgrounds as Fermi approached a zone in which there are high fluxes of charged particles. At the moment of the observation the Large Area Telescope LAT, the other bigger instrument on board, was already turned off, while GBM was almost on the border of its operation region. The good thing about the situation was that the source–GBM detector geometry was near optimal for the triggering detectors, allowing the measurement.
At the time of the GW170817 trigger none of the instruments on board to INTEGRAL, apart from the Anti-Coincidence Shield SPI-ACS, had substantial sensitivity in the direction of the source. This led to a reduced SPI-ACS signal significance and a lack of energy resolution [5].

As seen for GRB 170817 the several factors that can affect the GRB observations, together with the intrinsic unpredictable, short and unlocalised nature of the physical event, make the joint detection of gravitational waves and GRBs still rare.
The solution that we explore is the use of one or more nanosatellites to augment the sky coverage for GRB events. In particular, we focus on a CubeSat nanosatellite with a small detector onboard. It would have a large field of view and it would work in the MeV regime, from few keV to few MeV. In comparison to medium or big class missions, the nanosatellite's clear advantages are the small cost (approximately half a million Euros) and the rapidity of realization and launch (about one year). The low-costs makes the idea of more nanosatellites affordable and this aims at guaranteeing a full sky observation without interuptions e.g. Earth occultation, detector shutdown. From this point of view, the nanosatellites could play a key role in confirming and localizing the GRBs in response to alerts sent by other major detectors or detectors working with signals of different type. The proposal promises to reduce significantly the potential blind spots in our gaze to the sky in the MeV regime with a good ratio of performances versus needed resources.

The aim of the present work is to analyse the sensitivity that a future nanosatellite could reach; throught the use of simulations we are able to determine the performance of the detector with respect to the desired science objectives. In particular, Chapter 1 is an introductive overview of the physics involved, while Chapter 2 explains the method adopted to reach the target. Chapter 3 presents a more detailed analysis of two real GRB signals.

Chapter 1

GRB and MeV astrophysics

1.1 GRB

Gamma-Ray Bursts (GRBs) are short, intensive and non-periodic flashes of photons with energy principally in the gamma band. These extremely energetic explosions are among the brightest elettromagnetic events known to occur in the Universe. They were first discovered in the late sixties by the US military Vela satellite, whose mission was to monitor the "Partial Test Ban Treaty" that forbade nuclear explosions except underground. This discovery led to an intensive investigation of their origin, progenitor system and emission properties (energy peak, duration, spectral shape, variability timescale) which is still on-going. From the beginning the uniform distribution on the sky and the fluence distribution of the bursts pointed to a cosmological origin.

GRBs present a wide range of spectral and temporal properties and their defining feature among all the known astrophysical transients is their dominant, non-repeating, and non-periodic prompt gamma-ray emission. The phenomenology of GRB is described in terms of duration, variability, spectral parameters, fluence, peak flux, temporal and spectral evolution; correlations between these parameters are also remarkable.

The major breakthrough in the field came from the discovery of afterglows from long GRBs. At the end of the nineties the Italian-Dutch satellite Beppo-SAX measured the first fading emission that follows the prompt emission. The afterglows allowed the localization of the burst in lower energy band, such as X-rays, optical, infrared and radio, and led to redshift measurements. This demostrated their cosmological origin and implies that GRB sources are much more luminous than previously thought, assuming a total energy release of $E = 4\pi d^2 f$ (with d=distance from the source, f=observed fluence).

In the framework of a cosmological origin, the energy release is up to an isotropic-equivalent value of $\sim 10^{54}$ erg and the typical fluence of 10^{-7} up to 10^{-4} erg/cm^2 (lower limit is due to the characteristics of the detector) [17]. Such high energy values led to the hypothesis that the emission is strongly collimated in relativistic jets.

1.1.1 Short and Long GRB

GRB durations vary from a fraction of second to several hundreds of seconds. The prompt event is defined as the time-period when the gamma-ray detector measure a signal above the background, however the total duration of the burst is difficult to determined, due to the background emission. Therefore the most commonly diffuse measure is the T_{90}, the time within which 5% and 95% of the total number of counts has been detected. The T_{90} distribution highlights the clearest sub-classes of the GRBs population: the short-hard and the long-soft bursts.
Even though the burst hardness distribution shows a single population, a plot of the hardness vs temporal duration shows that the correlation between the two properties is significant. For this reason the GRBs belonging to the two different sub-classes are believed to originate from different progenitors: collapsars as the progenitors for long GRBs, and compact binary mergers as the progenitors for short GRBs.

The bimodal shape of the T_{90} distribution is well described by two log-normal trend with a first peak at ~ 0.2 s and a second peak at ~ 30 s [7]. Therefore we can define short bursts when $T_{90} < 2$ s while long bursts for $T_{90} > 2$ s.

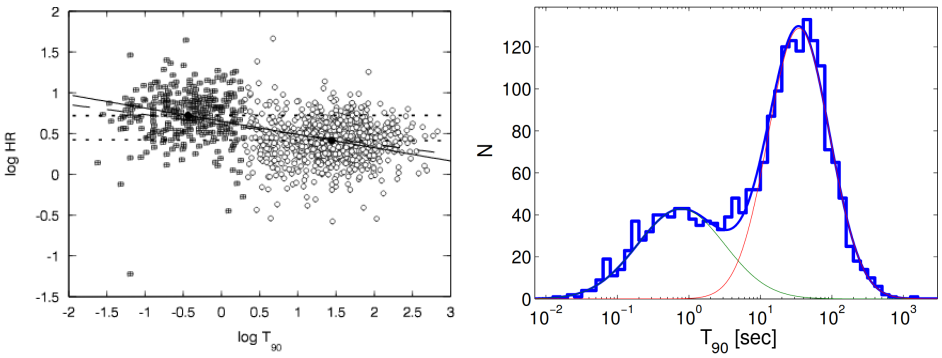

Figure 1.1: LEFT: hardness-duration correlation for BATSE bursts [9]. HR is the ratio of fluence between BATSE channels 3 and 2. RIGHT: duration distribution of 2041 bursts in the BATSE catalog [7].

1.1.2 GRB spectra

The observed spectra are non-thermal. An excellent phenomenological fit for the spectrum is the Band function [8]. This is composed by a low energy power-law (index α) with an exponential cut-off combined with a steeper power-law (index β, with $\alpha < \beta$) at high energy. There is no particular theoretical model that predicts this spectral shape. This function is used in Chapter 2.

$$f_{band}(E) = \begin{cases} A\left(\frac{E}{100keV}\right)^{\alpha} \exp\left[-\frac{(\alpha+2)E}{E_{peak}}\right] & E < \frac{(\alpha-\beta)E_{peak}}{\alpha+2} \\ A\left(\frac{E}{100keV}\right)^{\beta} \exp(\beta-\alpha)\left[\frac{(\alpha-\beta)E_{peak}}{100keV(\alpha+2)}\right]^{(\alpha-\beta)} & E \geq \frac{(\alpha-\beta)E_{peak}}{\alpha+2} \end{cases}$$

Other three possible spectral models are known for the measurable spectrum of GRBs depending on intensity. Less intense bursts (in the observer frame) provide less data to support a large number of parameters. That is why in many situations a particular empirical function provides a poor fit, while in other cases it provides an accurate fit. These models include a single power law (Pl), an exponential cut-off power law ("Comp"), and a smoothly broken power law (Sbpl). In particular the Comptonized model is an exponentially cut-off power law, which is a subset of the Band function in the limit that $\beta \to -\infty$.
For bright GRBs, the Band and Sbpl functions are a good description of the spectrum, while for weaker bursts the Comptonized function is the most appropriate. Bursts that have signal significance on the order of the background fluctuations are well described by the single power law function because of the lack of a detectable distinctive break in their spectrum.

Recently the Fermi LAT detector has established that a hard emission component (>40 MeV), in addition to a Band component, is found in the short hard class of GRBs. The first burst that shows strong evidence for a deviation from a Band spectral fitting function during the prompt emission phase is GRB 090510 [3]. Notably, its spectrum is fit by the sum of a Band function and a hard power-law component that dominates the emission below ≈20 keV and above ≈100 MeV.

1.1.3 GRB and gravitational wave events

Observations of short GRBs and their afterglows can shed light on the electromagnetic (EM) signatures that accompany gravitational wave sources detected by Advanced LIGO/Virgo [11]. The information that can be gained from the joint detection of gravitational waves and short GRBs is invaluable to establish the compact object merger model or to shed light on differences in the short GRB population that are due to the coalescence of double neutron star or neutron star-black hole binaries. Furthermore the properties of the EM counterparts will clarify the behavior of matter following the merger, namely accretion disks, jets, etc.

In addition, EM counterparts are essential for pinpointing the exact locations of the mergers: the typical localization region for the Advanced LIGO/ Virgo network (3 detectors) is ~ 100 deg^2 (this may improve with future detectors). This presents a unique challenge for EM follow-up, and for counterpart discrimination and identification, compared for example to studies of short GRBs from Swift, which are localized to better than a few arcminutes radius.

To fully unravel the astrophysical context of the event it is also important to take into consideration the fraction of observed GRBs followed by variable X-ray emission with a fluence comparable to, or in excess of the initial

burst.
Regardless of its origin, this provides an additional potential EM counterpart, especially if the X-ray emission is more isotropic than the GRB itself.

1.1.4 GRB observations

The launch of the Compton Gamma-ray Observatory (CGRO) dedicated mission, dated to the 1991, opened the BATSE era (1991-2000) from which came most of our basic knowledge [12]. The BATSE (Burst and Transient Source Experiment) was one of the four instruments on board of the CGRO, it made all sky survey and it showed that GRBs are isotropically distributed. The CGRO carried also COMPTEL, OSSE and EGRET instruments that, together with BATSE, covered an energy band from few keV up to 30 GeV.

During the last decade, several X- and gamma-ray satellites were launched: INTEGRAL (October 2002), Swift (November 2004), the italian AGILE (April 2007), Fermi (June 2008) are just some of the on-going observatories that are revolutionizing our understanding of GRBs.
The fundamental difference in the existing and future instruments is due to the specific aim for which they are designed: large Field Of View (FOV) detectors, suitable for scanning big region of the sky, are typically scintillators, while pointing detectors have technology based on cameras, pixel cameras or coded mask. Pointing telescopes usually manage to reach high performances but they need a quite accurate initial localization of the source; this can be provided by the large FOV telescopes.

An example of pointing detector is Swift [17], a multi-wavelenght satellite, carrying the BAT Burst Alert Telescope, a coded mask designed to monitor a large fraction of the sky, the XRT X-Ray Telescope, spectrometer designed to measure the position, spectrum and brightness of GRB and afterglows, and UVOT that, aligned with XRT, provides a simultaneous ultraviolet and optical coverage in a limited aperture. These three instruments work together to observe GRBs and their afterglows in the gamma-ray, X-ray, ultraviolet and optical wavebands and to accurately localize GRBs afterglows within tens of seconds from their discovery to enable rapid follow-up observations.
On the other hand, the Gamma-Ray Burst Monitor GBM [4], on board to GLAST, is a scintillator telescope working in the soft gamma-ray and X-ray energy range (8 keV – 40 MeV). The twelve Thalium-doped Sodium Iodide (NaI) scintillation detectors are pointed at various angles in order to survey the entire sky unocculted by the Earth at any time during the orbit and the two other detectors composed of Bismuth Germanate (BGO) crystals are placed on opposite sides of the spacecraft. GBM observes the entire sky not occulted by Earth.

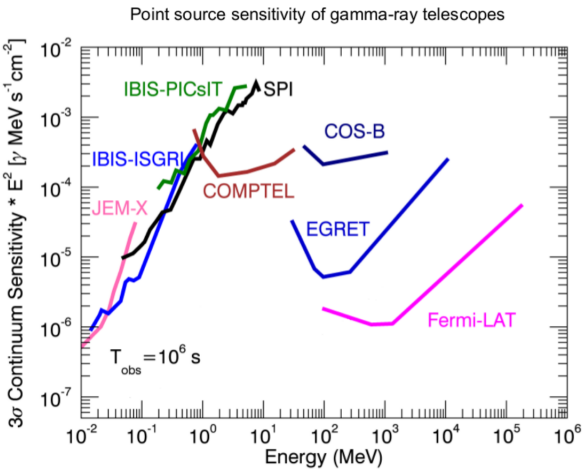

Figure 1.2: Continuum sensitivity of different detectors (with respect to a continuous spectral distribution).

1.2 MeV regime

Gamma-ray astronomy in the MeV regime detects photons in the energy range from a few hundred keV to ∼10 MeV. Here Compton scattering (CS) is the dominant interaction of photons with matter.
This energy range is also the region of nuclear decay lines, allowing us to investigate the chemical content of several astrophysical objects. Nuclear lines carry information about origin and distribution of individual isotopes in the cosmos, and in processes involving several cosmic sources like supernovae, novae, pulsars etc.

As previously reported, in the last few decades we have significantly expanded our X-ray and gamma-ray view of the sky, however a gap in coverage of the electromagnetic spectrum remains. The approximate transition point between X rays and gamma rays near 1 MeV is actually poorly explored mainly because of the modest sensitivity achieved by COMPTEL, the latest mission operating in this energy range (in the 1990s).
Considering Figure 1.2 it is clearly evident that COMPTEL sensitivity is not comparable to the sensitivities reached by later X and high energy gamma-ray observatories. Therefore it seems natural to look at a future Compton Telescope to investigate some fundamental science objectives in this energy range.

As said the Compton scattering is the dominant photon-interaction process at these energy for the majority of materials (cross-section depends on the atomic number Z of the scatter material). It consists in the elastic scattering of a photon by an electron and it can be described in terms of energy and momentum conservation of photon and electron. The relation between energies and Compton scatter angle φ can be derived:

$$cos\varphi = 1 - \frac{E_0}{E_g} + \frac{E_0}{E_g + E_e}$$

where E_0 is the rest energy of the electron, E_g is the energy of the scattered gamma ray and E_e the energy of the recoil electron.

The differential Compton cross-section for unpolarized photons scattering of unbound electrons was derived by Klein and Nishina in 1929. Clearly it constitutes only an approximation, since the electron is assumed not to be bound to an atom and to be at rest.

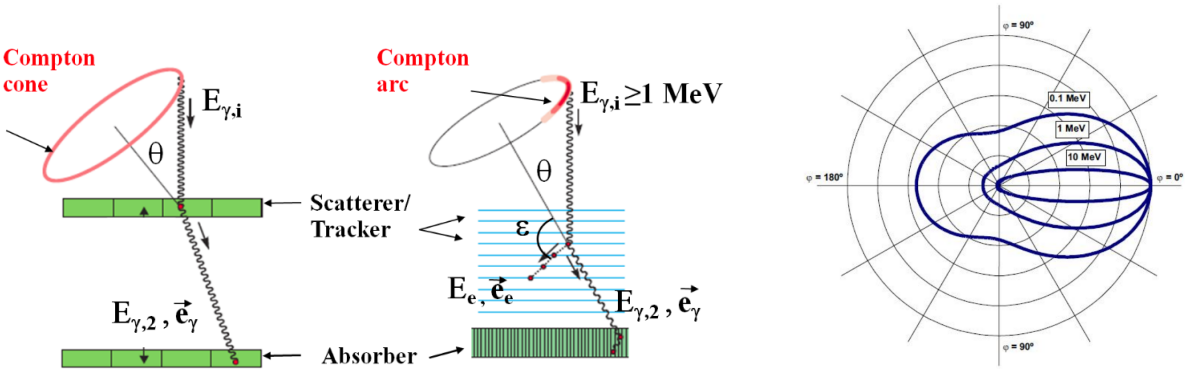

Figure 1.3: LEFT: COMPTEL type telescope vs Modern type Compton telescope. RIGHT: Klein-Nishina cross section as a function of angle and energy.

It is important to note that observations in this region are complex, for various reasons.
First, Compton scattering intrinsically implies a complex event recostruction process. Moreover, because of absorption from the Earth's atmosphere, it is necessary to place instruments in orbit. Even in a quasi-equatorial Low Earth Orbit (LEO) at ∼500 km above sea level a lot of factors contributes to cause a significant background. They are worth mentioning:

- Earth's gamma emission: the interaction between primary cosmic rays and the Earth's atmosphere generates secondary particles and a bright gamma-ray flux. Because the Earth's gamma emission flux is considerable in LEO, it usually represents the most significant background contribution in the MeV regime;
- Charged background: events due to charged cosmic rays hitting the detector, they are reduced with the use of an anticoicidence detector;
- Activation: the continuous flux of cosmic rays and hadrons in particular activates internally the satellite's materials producing, for example, radioactive isotopes that can decay and contaminate the spectra. Its contribution depends on the exact materials and geometry of the detector;
- Extra-galactic background: an isotropic and homogeneous photon background, mainly due to unresolved sources.

Two different quantities result fundamental to describe the angular resolution of Compton reconstructed events: the Angular Resolution Measure or ARM, and the Scatter Plane Deviation or SPD.

The ARM quantifies how precisely the direction of the scattered photon has been reconstructed and it is defined as:

$$ARM = \varphi - \varphi_{geo}$$

where φ is the computed Compton scatter angle and φ_{geo} the true scatter angle. The finite width in the distribution of the ARM measurement, centred around zero, is a measure of the uncertainty in the opening angle of the Compton cone.

SPD, relevant only if the track of the recoil electron is observed, quantifies how well the electron momentum is reconstructed and it is defined as the difference between the actual scatter plane and the measured one. More intuitively the scatter plane deviation describe the length of the Compton arcs and it is always equal to the maximum value of 180° for events in which the electron track is not observed.

1.2.1 COMPTEL

In the Mev regime, as of today, the telescope with the better sensitivity at 1 MeV is the concluded mission COMPTEL (Imaging Compton Telescope) [12], which worked in the range between 800 keV and 30 MeV.
The detector system is based on two fundamental components: D1, a low-Z scatterer consisting on seven modules filled with organic scintillator, and D2, a high-Z absorber made of fourteen modules of inorganic NaI(Tl) crystals. In the low-Z detector the Compton scatter interaction takes place while the high-Z detector absorbs the scattered photons. Each D1 and D2 modules are viewed by several photo-multiplier tubes (PMTs) and they are divided by a known distance of 150 cm so the Time-of-Flight (ToF) of the scattered photon between the two detectors can be measured.

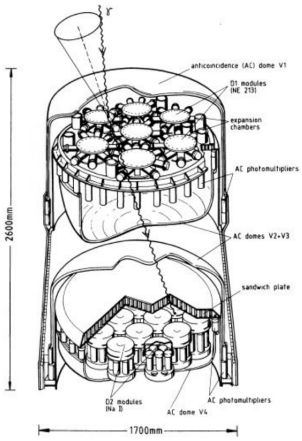

Figure 1.4: Schematic view of COMPTEL instrument.

The big mass of the whole structure of COMPTEL together with the fact that it was on board CGRO, a several tons mission, implies COMPTEL had a lot passive material, a source of background due to activation. On the other hand, the active mass provided a quite small effective area ranging from 10 to 40 cm^2, dependent on energy. In particular the effective area at 1 MeV was around 10 cm^2.

Notably, the data processing time scale for scintillators and PMTs is of the order of nanoseconds and the raw ToF values are used by the onboard electronics to distinguish top-to-bottom events (D1→D2) from bottom-to-top events (D2→D1). This results very useful for background rejection of the Earth's albedo, which comes from the atmosphere.

Finally it is worth to notice that with COMPTEL instrument it is not possible to measure the direction of the recoil electron, therefore only event cones are reconstructed, with no information on the event plane.

1.2.2 Future mission

Looking at the future of MeV investigations, we imagine a new era led by "Modern type" Compton telescopes, with a design inherited from Fermi-LAT, AGILE, Pamela etc.
The great innovation brought by a new group of detectors is the capacity of observing, for a fraction of the events, the direction of the recoil electron from the Compton scattering with a tracker. This enables a more accurate determination of the kinematic, reducing the Compton cone to a segment of the cone. For them only fewer photons are needed to recover the position of sources.
On the other hand, Silicon-based instruments have a slower readout time ($\sim \mu$s), making the discrimination of up- or down-going photons impossible.

Nowadays several Compton space missions have been proposed, such as the leading proposals for medium-class missions: e-ASTROGAM [14], and AMEGO [18]. The energy coverage spans the range from 200 keV to a few GeV, encompassing both Compton and pair-production regimes. These instruments will rely on Silicon strip detector technology and all of them promise substantial performance improvements relative to COMPTEL, such as higher energy and angular resolution and better sensitivity.
We highlight that such kind of proposals have time scale of about 10 years for the construction and a cost of hundreds of million Euros/Dollars.

1.2.3 CubeSat

In the more recent future another solution could be interesting: a Compton nanosatellite with contained development costs and that can potentially be launched very quickly.
In addition to the great impact that such small telescope could have in multi-messenger astrophysics (see Introduction chapter), a nanosatellite based on a scientific payload similar to the one proposed by the M-class missions can be also used as a pathfinder test instrument for the future telescopes. The nanosatellite that we take into consideration is a small CubeSat Telescope, with overall performance superior or at least similar to that of COMPTEL.

A CubeSat is a standardized model of miniaturized satellite with precise characteristics: it consists in a $10 \times 10 \times 10$ cm^3 cube with a maximum weight of 1.33 kg (1U cubesat). We use a 2U standard for the instrument so the total size is $10 \times 10 \times 20$ cm^3, estimating a 4U model in the final design with the on-board electronics and the flight system and a total mass of $\sim$3 kg [13].

The instrument will operate in the energy range from $\sim$100 keV up to few MeV and it is supposed to be orbiting in quasi-equatorial Low Earth Orbit.

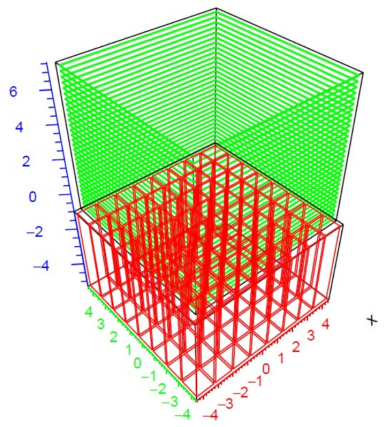

Figure 1.5: Schematic of the CubeSat geometry (anti-coincidence not shown).

The design of the nanosatellite, inspired from previous missions such as Fermi-LAT and AGILE, is composed by:

- 30 layers of Silicon, which constitute the tracker with the dimensions of $8.4 \times 8.4 \times 7.5$ cm^3 on the upper half of the structure;
- A calorimeter block made of an array of 8×8 Cesium Iodide CsI(Tl) bars on the lower half;
- 4 bars of Aluminum, which constitute the support structure located in the four corners;
- A Plastic scintillator anticoincidence, a box which covers the whole instrument and rejects nearly all the charged particle background.

Additional support structures for the tracker and calorimeter, and the readout electronics, are not included in the mass model yet.

For our nanosatellite, studies on its possible achivements have already been carried out by means of specific simulations. For more details [13].
Results are displayed in Figure 1.6. Tracked events presented larger ARM values than untracked ones. Nevertheless, tracked events have also a measurement of the scatter plane that helps in localizing the position of the source.

Performance in the pair-production regime was also estimated and found lacking, mostly due to the thin calorimeter.

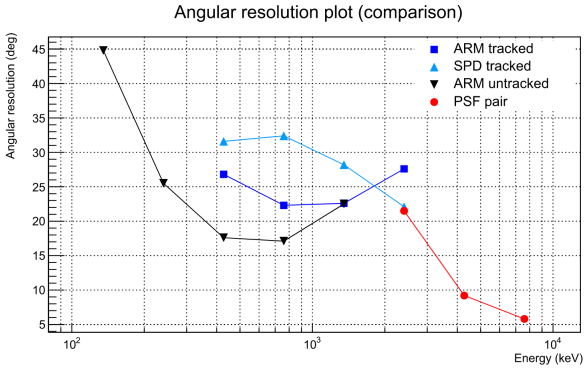

Figure 1.6: Estimated ARM and SPD for Compton events, and PSF for pair events.

Chapter 2

Method

The second part of the thesis is focussed on the study of the sensitivity that the CubeSat nanosatellite could achieve for GRB observations in the MeV regime, exactly we consider energy from 100 keV to 5 MeV.
The exact values we derive will depend on the exact formulation of the problem. In this work we assume that:

- we will have an alert, providing the start time and T_{90} of a GRB (it could be internally generated);
- we want to confirm the alert at 3-sigma significance;
- we want to provide a location of the GRB;
- the procedure could be automated to run unassisted.

The GRBs considered are part of the 3^{rd} Fermi GBM Gamma-Ray Burst Catalog [8] which concerns the first six years of observations and it gathers a list of 1405 triggers identified as GRBs. For each GRB the catolog supplies the location and main characteristics of the prompt emission such as the duration, peak flux and fluence; the latter is calculated using the suitable fitting function for the spectrum. The parameters for every models are given in the catalog and for this work we assume, for simplicity, a Band function for all the spectra.

2.1 MEGAlib simulations

The data analysis tool that we use to performe the simulations is the MEGAlib (the Medium Energy Gamma-ray Astronomy library) software package [16].
Its main application areas are telescopes ranging from a few keV up to tens of GeV. The process consists on four steps:

- Geomega (Geometry for MEGAlib) is the tool for geometry and detector description for the detailed modelling of different detector types;
- Cosima (Cosmic Simulator for MEGAlib) is the simulation tool based on Geant4. It simulates particle transport and interactions;
- Revan (Real Event Analyzer) reconstructs the event from the simulated hits and a parametric description of the electronics. The output is a list of events with the type of the first interaction (Compton, Pair, etc.) and a description of the event geometry (energy, direction for pair-production, axis, aperture, possibly event plane for Compton...);
- Mimrec (MEGAlib image reconstruction) is the main tool for advanced data analysis. Using a likelihood approach, it calculates a significance map in sky or instrument coordinates through a parametric description of the instrument response.

The essential result of MEGAlib simultations on which all the following analysis is based on is the image that represents the source distribution in terms of statistical significance value. This resource is obtained by the process of event reconstruction made by the Mimrec library. The selected imaging algorithm is called List-Mode Maximum-Likelihood Expectation-Maximization and it finds that source distribution which has the highest probability to generate the data, finding the maximum of a likelihood function. This developed algorithm naturally allows to incorporate all different event types (both tracked and untracked event as well as pair events) into one image.

2.2 Preparation to analysis

The method adopted for all the analysis follows.

1. We simulate with Cosima a defined source for a prearranged duration time. The parameters given in input to define the source are a file with the spectrum, as a list of data points, the photon flux integrated in an energy range and the position of the source in the satellite coordinates.
   In order to have a significant statistical sample, we choose a duration 100 or 1000 times longer than the real duration of the event. Then we cut the simulation in segments with the proper time length.

2. For each segment we create a reconstructed sky image with Revan and Mimrec. As already mentioned, the image is given as a map of statistical significance of the origin of the simulated events, in function of the angular coordinates in the reference system of the nanosatellite. Specifically, θ is the zenith angle while φ is the azimutal one. Given that Mimrec needs the detector response, in the simplest approach, we use only SPD and ARM modelled as gaussian distribution of which we take the standard deviation (the same for all events so we neglet the dependence e.g. on energy and on the inclination angle).

3. We locate the maximum significance for each simulation, and we draw an histogram to visualize the distribution of the maximum for the entire sample. We find also the angular coordinates of each maximum.

To follow the previous methodology we modified several scripts in Python that were developed for the study of the performance of the CubeSat.

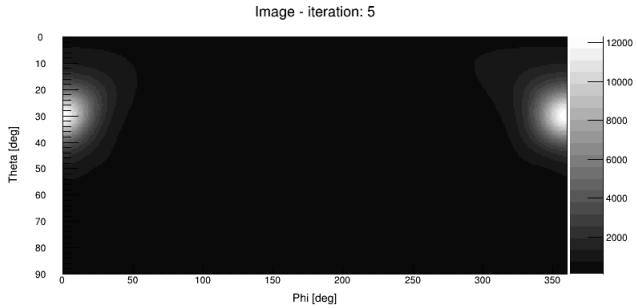

Figure 2.1: Mimrec reconstruction for 50 s simulation of GRB 090510.

As said, the reconstruction of the image from Mimrec needs an estimation of the ARM and SPD values. We choose to use measure deduced from an albedo simulation because the initial hypothesis for the satellite is to scan a sky in which only background is present. The running time chosen was 1000 s.
We do not appy any background rejection or event quality cuts.
In particular, the ARM was found as the sigma of a gaussian fit of the ARM distribution: $sigma = (9.7 \pm 0.2)°$; we did not take into consideration the tails of the distribution but only the central peak.
For the SPD, because of its symmetric distribution between 0° to 180°, the value was extimated by computing the standard deviation of the sample, assuming 0° as the mean:
$\sigma_{SPD} = \sqrt{\frac{\sum spd \cdot spd}{N}} = 34.07°$.

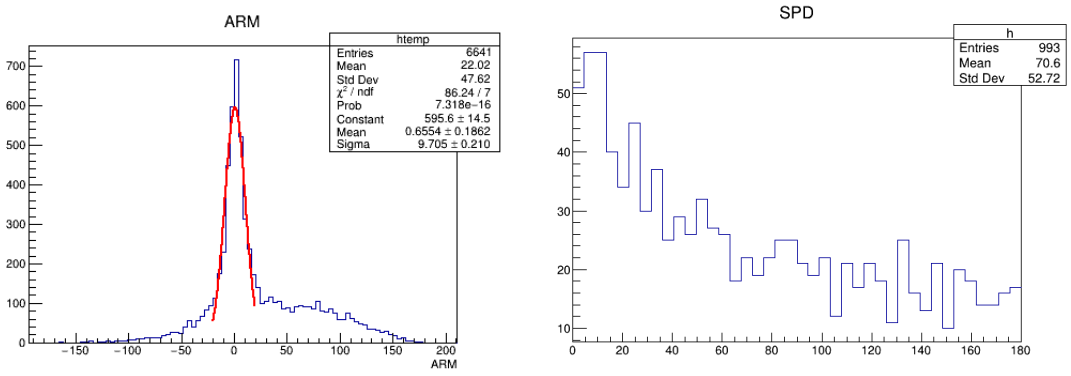

Figure 2.2: LEFT: ARM distribution from albedo simulation with gaussian fit. RIGHT: SPD distribution from albedo simulation for tracked events.

The Field Of View of the instrument is very large and it extends at inclinations larger than 90°. The final FOV will be defined by background rejection cuts and event quality cuts, which are not defined yet. At this stage we limit the phase space of the θ coordinate in the range [0°,90°] keeping clear of the bright Earth limb at 112° from the zenith.

For the simulations we use the Earth's albedo spectrum supplied by MEGAlib, compatible with the models used by e-ATROGAM and AMEGO.
Besides Earth's albedo, as said, other factors contribute to the total background, such as charged particles that can be largely avoided by the use of an anticoincident detector. Given that these additional contributions are almost one order of magnitude smaller than the albedo, we neglet them in this work.

2.3 Fermi GBM catalog

GRB simulations are based on the 3^{rd} Fermi GBM Gamma-Ray Burst Catalog which describes 1405 events with their defining features such as the T_{90}, fluence and fitting parameters for different spectrum models. To analyse the population, we choose to divide the GRBs into several subsets depending on their emission duration (T_{90} value).

Band Name	T min [s]	Tmax [s]	Simulated T_{90} [s]	Band Name	T min [s]	Tmax [s]	Simulated T_{90} [s]
band 1	1	2	2	band 7	64	128	128
band 2	2	4	4	band 8	128	256	256
band 3	4	8	8	band 9	0.125	0.25	0.25
band 4	8	16	16	band 10	0.25	0.5	0.5
band 5	16	32	32	band 11	0.5	1	1
band 6	32	64	64	band 12	-	0.125	0.125

Table 2.1: Band suddivision of Fermi GBM catalog

When simulating GRBs (see section 2.3.2.) we use the upper time bound of each band as the duration of our GRB.
It is important to note that the catalog reports for each GRB the value of its fluence given in erg/cm^2 integrated in the energy range from 10 keV to 1000 keV. This is not the energy range that we are interested to study: as said the CubeSat is efficient in the energy range from 100 keV to 5000 keV. Therefore, assuming a Band function for all the GRB spectra and getting the exact parameters for the function from the catalog, we compute the photon flux in ph/cm^2/s in the desidered range.

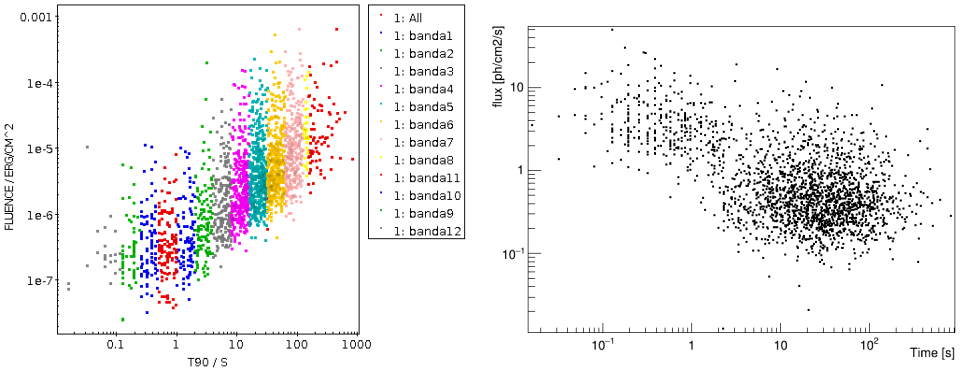

Figure 2.3: LEFT: plot of fluence [erg/cm^2] vs T_{90} of the GBM catalog, the band suddivision is highlighted. Energy range: 10 keV-1000 keV. RIGHT: plot flux [ph/cm^2/s] vs T_{90}, obtained from calculations. Energy range: 100 keV-5000 keV.

It is worth to notice how the distribution of the points is almost reverse in the two plots. From the first plot we see that short GRBs generally have lower fluences than those of long bursts, this is naturally due to their shorter durations, tipically < 2 s. On the other hand, in the second plot which represents the photon flux in time unit, the higher values corrispond to short GRBs.

2.3.1 Background cut-off

In accord to the band suddivision considered before, we study the background expected for each subset through the simulations.
We simulate albedo events for a total duration of 100000 s and we cut the reconstructed image in segments with a time duration equal to the selected band. We create a sample of 1000 segments for each band, a part for band 8, the longer one, for which only 780 segments were available.
For each sample we find the maximum significance and we draw the histrograms with the maximum distribution.

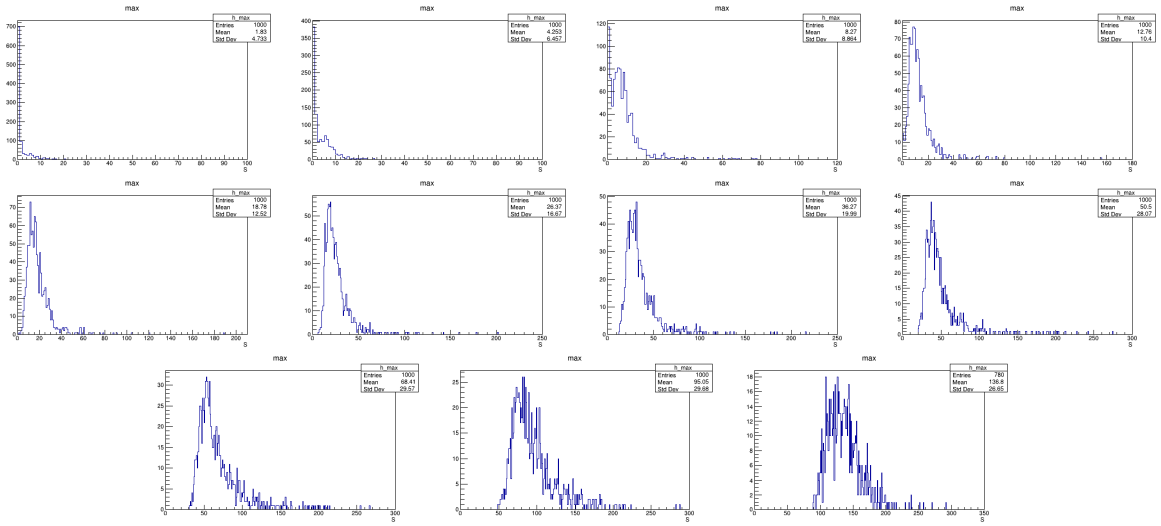

Figure 2.4: Histograms of maximum significance distribution of the albedo ordered for increasing time band ($\theta < 90°$).

As expected, increasing with the observation time, the peak in the maximum distribution moves to higher significance value.

At this point, we try to evaluate a raw limit of significance to distinguish between a possible signal and its background. We compute, using an adequate scripts, for each distribution the value, namely the percentile, for which the cumulative distribution function equals to 0.997 ("3σ significance").
From the histograms, we see that for the samples constituded by exactly 1000 values, the searched percentile, the cut-off from now on, coincides with the third to last value with the maximum significance. Clearly from the point of view adopted, the larger the statistical sample is, the better the evaluation of the cut-off value will be. For this preliminary work, we keep this limited statistics to restrict the time for simulation and reconstruction. To estimate the uncertainty, we compute also the percentiles adding and removing 0.1% from the original relative cumulative frequency of the cut-off. Again, better statistics is recommended for the future. Results are displayed in Table 2.2.

Simulated Time [s]	cut-off [S]	$q_{0.996}$ [S]	$q_{0.998}$ [S]
0.125	40	27	62
0.25	62	51	67
0.5	67	66	74
1	73.5	72	78
2	103	89	119
4	158	141	177
8	181	177	184
16	226	211	241
32	213	210	253
64	222	215	281
128	257.7	251.9	270.4

Table 2.2: Cut-off and range

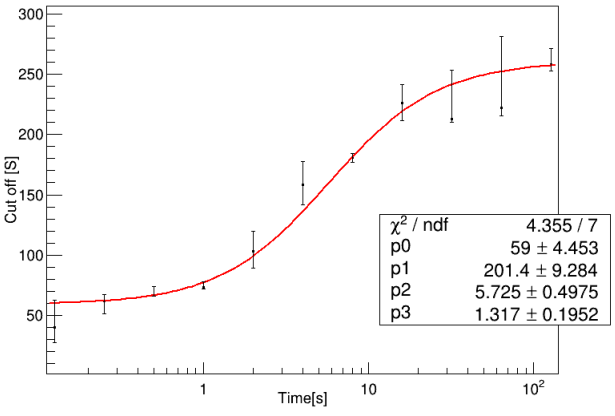

Figure 2.5: Fermi function fit of cut-off vs observing time

To better model the trend of the background cut-off as a function of the observing time, we fitted the data with

an empirical function. A function that well reproduces the data is the Fermi function:

$$f(t) = p0 + \frac{p1}{1 + e^{-\frac{t-p2}{p3}}}$$

The χ^2 test of the fit is remarkable: the compatibily value between the computed chi square and the degrees of freedom results $\lambda = \frac{|\chi^2 - ndf|}{\sqrt{2ndf}} = 0,7$.

The function choice was phenomenological: the Fermi profile well described the tendency to saturation of the cut-off values both for smaller and longer observing time and the growing trend for intermediate time.

As we expected, for the shortest time scales we approach a background-free region, followed by a rapid increase in the cut-off significance due to random coincidences in the background events, followed by a more stable regime with a slowly increasing, almost uniform background flux.

2.3.2 GRB simulations

Having modelled the background, we have to estimate the minimum flux for a GRB to be detected above the estimated threshold.
Again we study the GRB population of the 3^{rd} Fermi GBM Gamma-Ray Burst Catalog, with the suddivision described in Table 2.1 and we see a large variation in the spectral parameters for the different time band. Therefore we simulate two representative GRBs in each band, to have at least some estimate of the dependence on the spectral parameters. A more careful (and complex) approach would be to simulate all GRBs in the catalog as they are, and evaluate the significance of each.
We locate all the GRBs at $\theta = 30°$; the dependency of response and background with θ is small and it is negleted for now. We assume a Band spectral function, which well fits the great majority of the spectra, and we compute it using the fitting parameters of the catalog. As reported in Chapter 1, the needed parameters for the Band function are the two power-law indices α and β, the amplitude A and E_{peak}, the peak energy.
While for the parameters α, β and A the range of variation in each band was quite restricted, the value of peak energy resulted to vary over more than four orders of magnitude. In particular, as shown in Figure 2.6, the peak energies are well described by a gaussian distribution. Therefore we decided to simulate for each band both a signal with low and high value of E_{peak}, keeping the other parameters unchanged. Specifically, we calculate the peak energy value corrisponding to 0.5 and 0.9 of the gaussian cumulative distribution of $log(E_{peak})$; the former, which is the mean of the normal fit, results equal to 177 keV, while the latter is 741 keV and it is a peak energy rappresentative of the 10% of hardest GRBs.
The choice of having two representative GRBs in each band at different E_{peak} is due to the strong correlation with the detector efficiency, which depends strongly on the event energy [2].
For all other spectral parameters we take an average value computed for all GRBs in the considered time band.

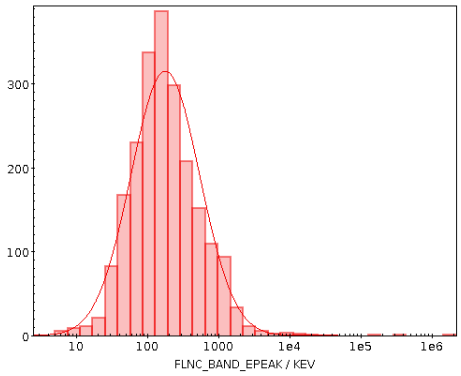

Figure 2.6: Gaussian distribution of $log(E_{peak})$ values for all GRB population.

To limit the statistical fluctuations, we simulate a GRB with ten times the average flux, we evaluate its statistical significance and analitically scale the flux to have the significance equal to the background cut-off value. In this view, the statistical errors for the ten times bigger significance were not computed.
For each simulation, we create the reconstructed sky with Mimrec and we individualize the maximum significance.

The basic assumption made was that the nanosatellite works in a proportional region between the detector's counts, which are traslated into a significance value, and the effective number of photons hitting the detector. We verified this assumption with the simulations.

t90 [s]	Max S for E_{peak}=177 keV	Max S for E_{peak}=741 keV
0.125	13	221
0.25	45	602
0.5	392	2787
1	391	4050
2	755	6938
4	919	6278
8	3066	21725
16	755	4279

Table 2.3: Results of GRB simulations.

We compute the ratio between the maximum significance of a signal and the cut-off of a background distribution for an equal observation time and then we traslate in terms of photon flux: $\Delta = \frac{maxS}{cut-off} = \frac{k \cdot 10 \cdot flux}{k \cdot flux - limit}$, remembering that the simulation concerns a signal ten times bigger. Reversing the formula, we find two limits photon flux for each simulated band: one relative to GRBs with E_{peak} around 177 keV and the other relative to signals with E_{peak} around 741 keV.

2.4 Results

The results of the analysis are displayed in Figure 2.7 where the photon flux limits for each band are drawn as horizontal lines, that separate the detactable from the undetectable GRBs for CubeSat.
In the Figure, black dots represent GRBs having $E_{peak} < 177$ keV, red dots with 177 keV$< E_{peak} <$ 741 keV while blue dots $E_{peak} > 741$ keV. Therefore, the blue horizontal lines corrispond, from our point of view, to the minimum flux that hard blue GRBs should have to be detected by CubeSat; equally the red lines are the minimum flux concerning signals coloured in red. As expected, in each band, that means for a fixed observing time, the limit value for the red population is higher than the blue one since the albedo distribution is equal.

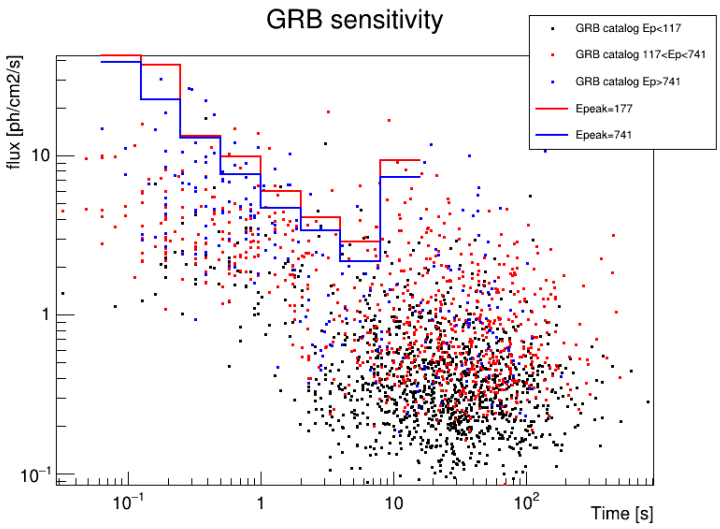

Figure 2.7: GBM catalog with sensitivity lines for CubeSat.

Notably, we see that the trend of the sensitivity bars clearly change slope at $T_{90} = 8$ s: to our analysis, the CubeSat nanosatellite is more efficient in detecting GRBs having a duration around that. On the other hand, both for longer and shorter time the ratio between the signal and the albedo significance is less favorable for the detection. The reason is that for short time the small detector measures only a few signal events while for longer time the background become significant.

As said, this is the results of a first analysis, with quite restrictive rules and without any kind of background rejection or quality cuts. Under this conditions, we esteem that CubeSat see approximately fourty GRBs in six years of work, which means a little less than seven signal per years. Of these fourty signals, more than the half are "blue hard" dots with T_{90} shorter or equal to a second.

As forecasted, the nanosatellite works better with short and hard GRBs which are the one more likely associated to gravitational vawes.
We remark that our estimate should be corrected by the possible difference in the FOV between CubeSat and GBM. At this stage, we do not take into consideration this discrepacy given that the final FOV of CubeSat has not been definied yet.

Chapter 3

Remarkable GRBs

In this final chapter we test the previous results with a more detailed analysis of two notable GRBs, a faint one and a bright one.

3.1 GRB 090510

GRB 090510, with a Band peak energy of 3.9±0.3 MeV, is undoubtedly one of the hardest GRBs seen by both Fermi GBM and LAT and it is the first short burst that shows strong evidence for a deviation from a Band spectral fitting function during the prompt emission phase. Specifically, spectral fits reveal a hard power-law component detected by LAT 0.1 s after the onset of the main prompt emission in the GBM band. This unexpected component dominates the emission below ∼20 keV and above ∼100 MeV.
These characteristics make GRB 090510 very interesting for studying high-energy emission models in the short hard class of GRBs.

In our work we take into consideration the emission time from T_0+0.5 s to T_0+ 1.0 s, settling at T_0 the precursor event that caused the GBM trigger, and we neglect the hard power-law component in the spectra which is out of CubeSat energy range. The Band parameters are: $E_{peak} = 4.104^{+0.267}_{-0.263}$ MeV, $\alpha = -0.75^{+0.03}_{-0.02}$, $\beta = -2.40 \pm 0.04$ and $A = (4.316^{+0.116}_{-0.115}) \cdot 10^{-2}$ cm^{-2}s^{-1}keV^{-1}.
Given that a real signal is always simultaneously detected with background noise, we simulate together the GRB and the albedo, using their respective differential energy spectra, for a total time of 50 s, from which we extrapolate a sample of 100 segments lasting 0.5 s. The position of the source in the reference system of the nanosatellite was established at the arbitrary angular coordinates of $(\varphi; \theta) = (0°; 30°)$.
Then, we compare the resulting maximum significance histogram with an albedo maximum significance distribution for the same time scale. For the comparison we normalise the two histograms.

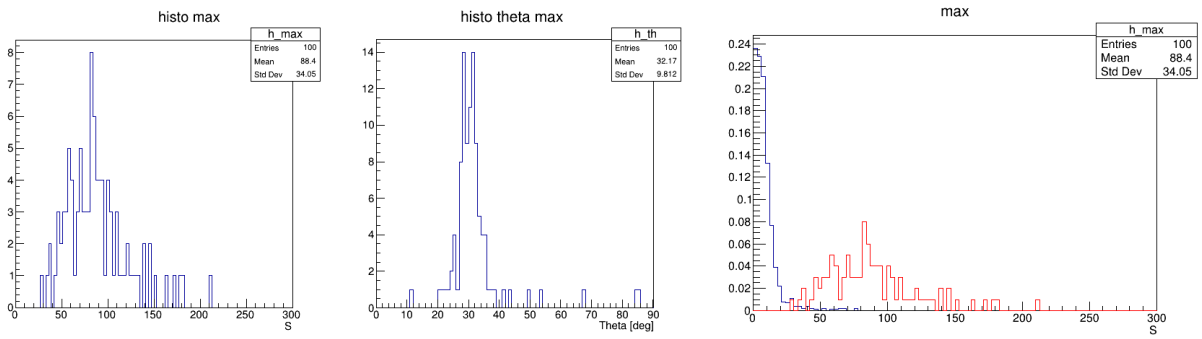

Figure 3.1: LEFT: Maximum significance histogram for GRB 090510. CENTRE: Histogram of the theta coordinates of the maximums. RIGHT: normalised maximum histograms of GRB signal (red) and background (blue).

As we see from the Figure 3.1, the maximum distribution of the signal and the noise are only slightly overlap and the raw mean value of the signal distribution ∼88 is largely above the cut-off significance computed, in the previous chapter, for this observation time at 67. According to the simulations and the methodology studied, GRB 090510 would have been very likely detected and correctly recognised by a CubeSat nanosatellite.

It is worth to notice that the fluctuations in significance of the GRB signal is quite large, having a standard deviation $\sigma = 34.05\ S$. By checking the simulation output file the average number of photons which contributes to create the signal, we find a distribution with mean value ~ 40 and standard deviation ~ 6, that well follows a Poisson distribution. This level of statistical fluctuation is well below the one observed in the histogram of significance above.
We conclude that some additional cause of fluctuation is present. A possible reason is the very simple model of the detector response we used, which can cause an incorrect estimate of the likelihood.
The localization capability of CubeSat is adequate, having a standard deviation of $\sim 10°$.

3.2 GRB 170817

The second GRB that we consider is the faint GRB 170817, which corrisponds to the first coincident observation of gravitational waves and electromagnetic radiation.
It is worth to underline that most of its energy was below ∼100 keV, apart from a short-hard initial pulse emitting at least up to 200 keV. As a consequence, this signal is almost on the limit of CubeSat energy range and therefore, we expect that the nanosatellite will not be the perfect detector for its observation.

We fit its spectrum for a duration time of 256 ms with an exponentially cut-off power law, namely Comptonized, which is a subset of the Band function in the limit that $\beta \to -\infty$. The parameters that we use are E_{peak}=215±54 keV and the power-law index of 0.14±0.59. To obtain the amplitude A, we use the information about the average energy flux over the GBM interval of 10–1000 keV that is $(5.5\pm1.2)\times10^{-7}$ erg/s/cm^2 and the corresponding fluence of $(1.4\pm0.3)\times10^{-7}$ erg/cm^2. Again we fix $(\varphi;\theta) = (0°;30°)$.

The simulation process was the same as GRB 090510, and we compare the resulting maximum significance histogram with an albedo distribution realtive to an observation time of 0.25 s.

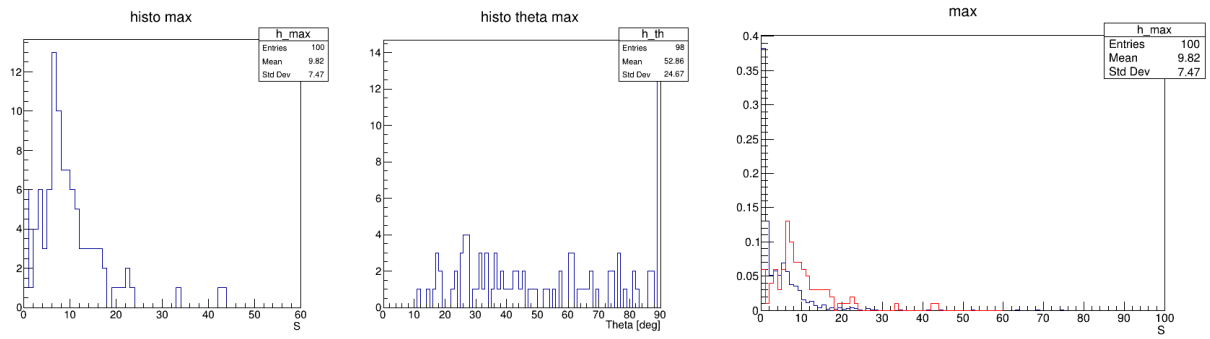

Figure 3.2: LEFT: Maximum significance histogram for GRB 170817. CENTRE: Histogram of the theta coordinates of the maximums. RIGHT: normalised maximum histograms of GRB signal (red) and background (blue).

In this case, we notice that the raw mean of the signal maximum significance distribution is ∼10 and it is largely below the cut-off value for the background of such time scale, which was found at 62. Therefore, it is clear that the methodology previously studied will not have recognised the signal of GRB 170817. As we can see from the figure, the albedo and the signal distributions are sufficiently overlapped and this fact makes such a simple analysis, based on the comparison between maximum significance values, useless for the detection.

Conclusions

The recent status of multi-messenger astrophysics suggested us a CubeSat nanosatellite, as MeV detector pathfinder for next proposals of mission. In particular we evaluated its performances for GRB observations seen the satellite as an aid in confirming and localizing a multi-messenger event.

In this work, we found that the nanosatellite could detect and localize approximatly 7 signals per year. These signals will be more likely short hard GRBs, which are the main candidates as electromagnetic counterparts of gravitational vawes. Trivially, such an expected number doubles using two detectors orbiting with a relative phase of 180°. As said, the low-cost of CubeSat makes affordable the idea of realizing and launching more detectors that could work together. For comparison, we report that big size missions are expected to detect approximatly 80 short GRBs per year. The price to be paid for such performances is a time scale ten times longer and a cost hundreds times higher than for CubeSat.

Future activities could perfect the results obtained in this thesis. As underlined, a more accurate evaluation could be achieved by increasing the simulated statistical sample and by defining the final Field Of View of the detector. In addition, the analysis of the observed GRB population would provide a better estimate of the expected rate of observations per year. For such a work, an automated pipeline will be needed.
Finally, the next steps in understanding CubeSat performances will require an evaluation of possible background rejection and quality cuts for the analysis. These considerations will very likely improve the sensitivity of CubeSat together with allowing a definition of its Field Of View.

Bibliography

[1] F. Berlato, *Design and optimization around 1 MeV of a calorimeter for a CubeSat Mission*, Master Thesis, Università degli Studi di Padova, 2016.

[2] G. Lucchetta, *Design and optimization around 1 MeV of a Tracker for a CubeSat Mission*, Master Thesis, Università degli Studi di Padova, 2016.

[3] M. Ackermann et al., *Fermi Observations of GRB 090510: A Short Hard Gamma-Ray Burst with an Additional, Hard Power-Law Component from 10 keV to GeV Energies*, Astrophysical Journal, 2010.

[4] A. Goldstein et al., *An ordinary short gamma-ray burst with extraordinary implications: Fermi-GBM detection of GRB 170817A*, Astrophysical Journal Letters, 2017.

[5] V. Savchenko et al., *INTEGRAL Detection of the First Prompt Gamma-Ray Signal Coincident with the Gravitational-wave Event GW170817*, The Astrophysical Journal Letters, 2017.

[6] E. Berger, *Short-Duration Gamma-Ray Bursts*, Annual Review of Astronomy and Astrophysics, 2013.

[7] E. Nakar, *Short-Hard Gamma-Ray Bursts*, Physics Reports, 2007.

[8] P. Narayana Bhat et al., *The Third Fermi GBM Gamma-Ray Burst Catalog: The First Six Years*, The Astrophysical Journal Supplement Series, 2016.

[9] T. Piran, *The physics of gamma-ray bursts*, Reviews of Modern Physics, 2004.

[10] T. Piran, *Gamma-ray bursts and the fireball model*, Physics Reports, 1999.

[11] B.D. Metzger, E. Berger, *What is the Most Promising Electromagnetic Counterpart of a Neutron Star Binary Merger?*, The Astrophysical Journal, 2012.

[12] V. Schönfelder et al., *Instrument description and performance of the imaging gamma-ray telescope Comptel aboard the Compton Gamma-ray Observatory*, The Astrophysical Journal Supplement Series, 1993.

[13] G. Lucchetta et al., *Scientific Performance of a Nanosatellite MeV Telescope*, The Astrophysical Journal, 2017.

[14] A. De Angelis et al., *The e-ASTROGAM mission (exploring the extreme Universe with gamma rays in the MeV – GeV range)*, Experimental Astronomy, 2017.

[15] A. Zoglauer, *MEGAlib - Simulation and Data Analysis for Low-to-medium-energy Gamma-ray Telescopes*, 2008.

[16] A. Zoglauer, *First Light fot the next generation of Compton and Pair telescopes*, PHD Thesis, Technische Univesitat Munchen, 2005.

[17] S.Cutini, *Study of X-ray and γ-ray emission from Gamma-ray bursts and their afterglows*, PHD Thesis, Università di Perugia.

[18] https://asd.gsfc.nasa.gov/amego